

Supporting Information

Formation of a quasi-solid structure by intercalated noble gas atoms in pores of Cu^I-MFU-4*l* metal-organic framework

Oxana V. Magdysyuk, Dmytro Denysenko, Ingrid Weinrauch,
Dirk Volkmer, Michael Hirscher, and Robert E. Dinnebier

Table of Contents

Gas sorption measurements.....	2
Thermal Desorption Spectroscopy of Xe and Kr in Cu ^I -MFU-4 <i>l</i>	7
Lattice parameters and total amount of adsorbed atoms per unit cell for Xe adsorption in Cu ^I -MFU-4 <i>l</i>	9
Lattice parameters and total amount of adsorbed atoms per unit cell for Kr adsorption in Cu ^I -MFU-4 <i>l</i>	9
Atomic positions and occupancies of intercalated Xe atoms in Cu ^I -MFU-4 <i>l</i>	10
Atomic positions and occupancies of intercalated Kr atoms in Cu ^I -MFU-4 <i>l</i>	11
Rietveld plots of Cu ^I -MFU-4 <i>l</i> with different amount of adsorbed Xe and Kr.....	12

Gas sorption measurements

The sample of Cu^I-MFU-4*l* was prepared in situ from Cu^{II}-MFU-4*l*-formate by heating for 1 h at 180 °C under vacuum and degassed for 2 h at 150 °C between the measurements under high vacuum ($P < 10^{-4}$ mbar). Adsorption isotherms were measured with a BELSORP-max instrument combined with a BELCryo system. For the determination of isosteric heats of adsorption in Cu^I-MFU-4*l*, four isotherms at 220, 230, 240 and 250 K for Kr and at 280, 290, 300 and 310 K for Xe were measured (Figures S1-2). The isosteric heats of adsorption were calculated from the measured isotherms using the Clausius-Clapeyron equation (I). The slopes of linear plots lnP versus 1/RT for different loadings (Figures S3-4) give the adsorption enthalpies, according to the equation (II).

$$Q_{st} = -R \left(\frac{\partial(\ln P)}{\partial(1/T)} \right)_{\theta} \quad (\text{I}), \theta - \text{surface coverage}$$

$$\ln P = -\frac{Q_{st}}{R} \left(\frac{1}{T} \right) + C \quad (\text{II}), C - \text{integration constant}$$

The isosteric heats of adsorption at zero limit surface coverage (initial heat of adsorption) have been determined using Henry's constants K_H , obtained as a slope from the linear ranges of isotherms at low pressure (Tables 1-2 and Figures S5-6). In this range the dependence of amount adsorbed (n) on the pressure can be expressed with Henry's law (III). The initial isosteric heat of adsorption can be obtained in a similar way by using the Clausius-Clapeyron equation (IV) (Figure S7).

$$n = K_H \cdot P \quad (\text{III})$$

$$\lim_{n \rightarrow 0} (Q_{st}) = Q_{st}^0 = R \left(\frac{\partial(\ln K_H)}{\partial(1/T)} \right) \quad (\text{IV})$$

Table S1. Henry's constants for Kr adsorption in Cu^I-MFU-4*l*, cm³ g⁻¹ kPa⁻¹

T, K	220	230	240	250
K _H	1.0158	0.696	0.501	0.3655

Table S2. Henry's constants for Xe adsorption in Cu^I-MFU-4*l*, cm³ g⁻¹ kPa⁻¹

T, K	280	290	300	310
K _H	1.0282	0.7517	0.5663	0.4371

Table S3. Loading-dependent isosteric heats for Kr and Xe adsorption in Cu^I-MFU-4*l*, kJ mol⁻¹

Loading / mmol g ⁻¹	Kr	Xe
0*	15.5	20.6
0.18	15.0	-
0.36	14.4	19.1
0.54	14.0	19.0
0.71	14.0	18.9
0.89	14.3	18.9
1.07	-	18.9
1.12	13.9	-
1.25	-	18.9
1.34	13.6	-
1.43	-	19.0

* Determined from Henry's constants.

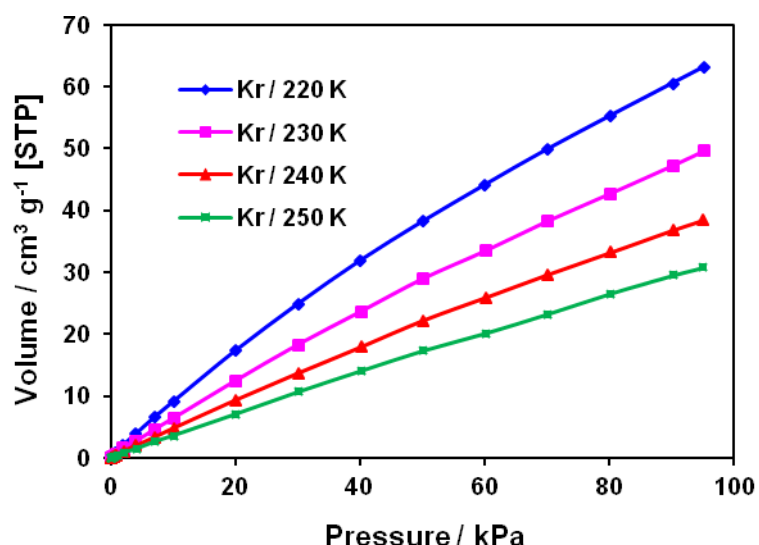


Figure S1. Kr adsorption isotherms for Cu^I-MFU-4*l*.

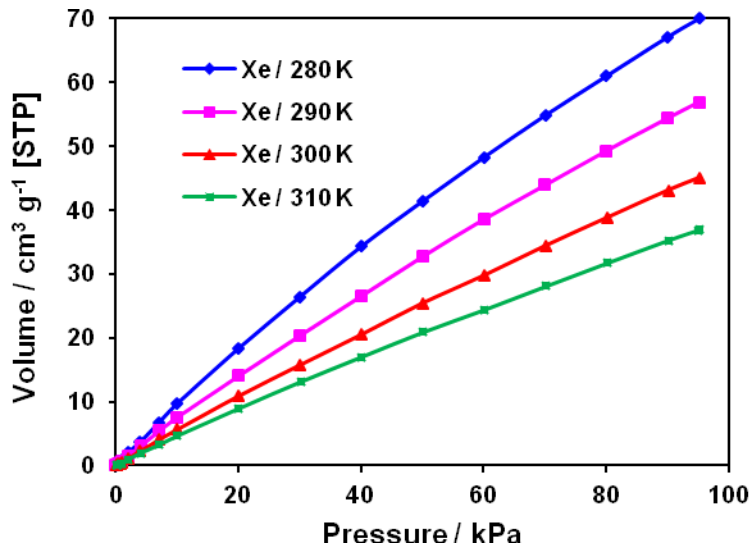


Figure S2. Xe adsorption isotherms for Cu¹-MFU-4*l*.

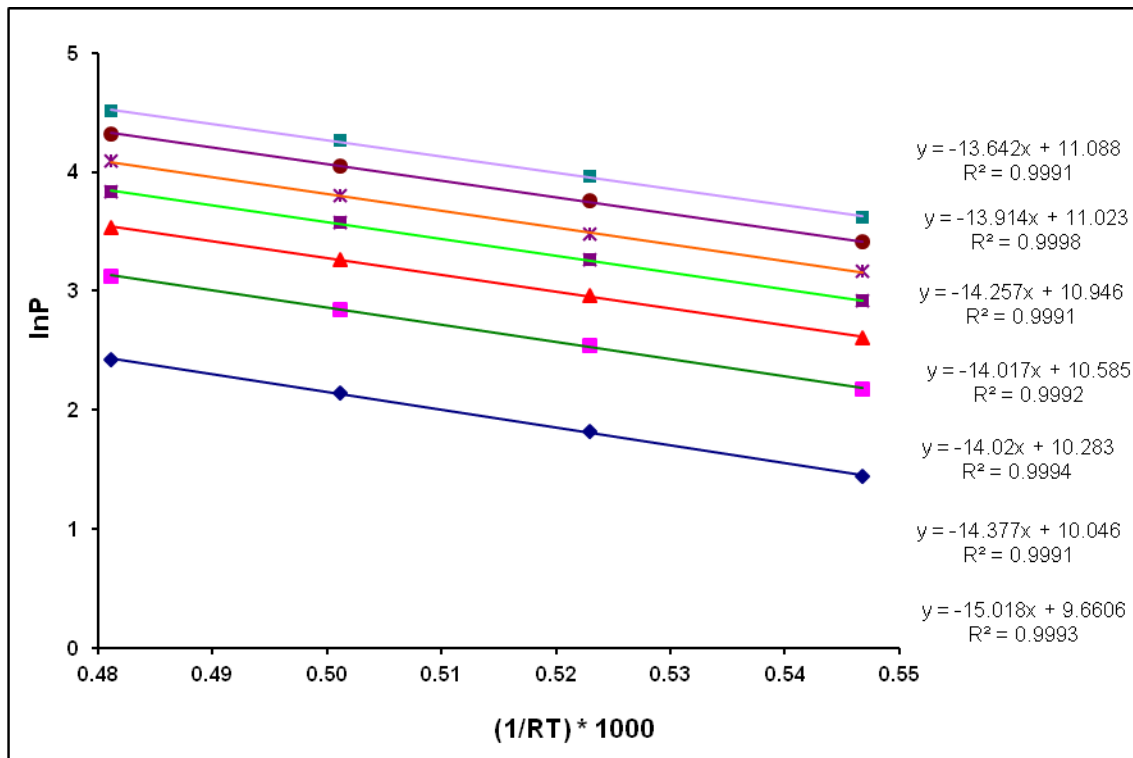


Figure S3. lnP versus 1/RT plots for different loadings for Kr adsorption in Cu¹-MFU-4*l*.

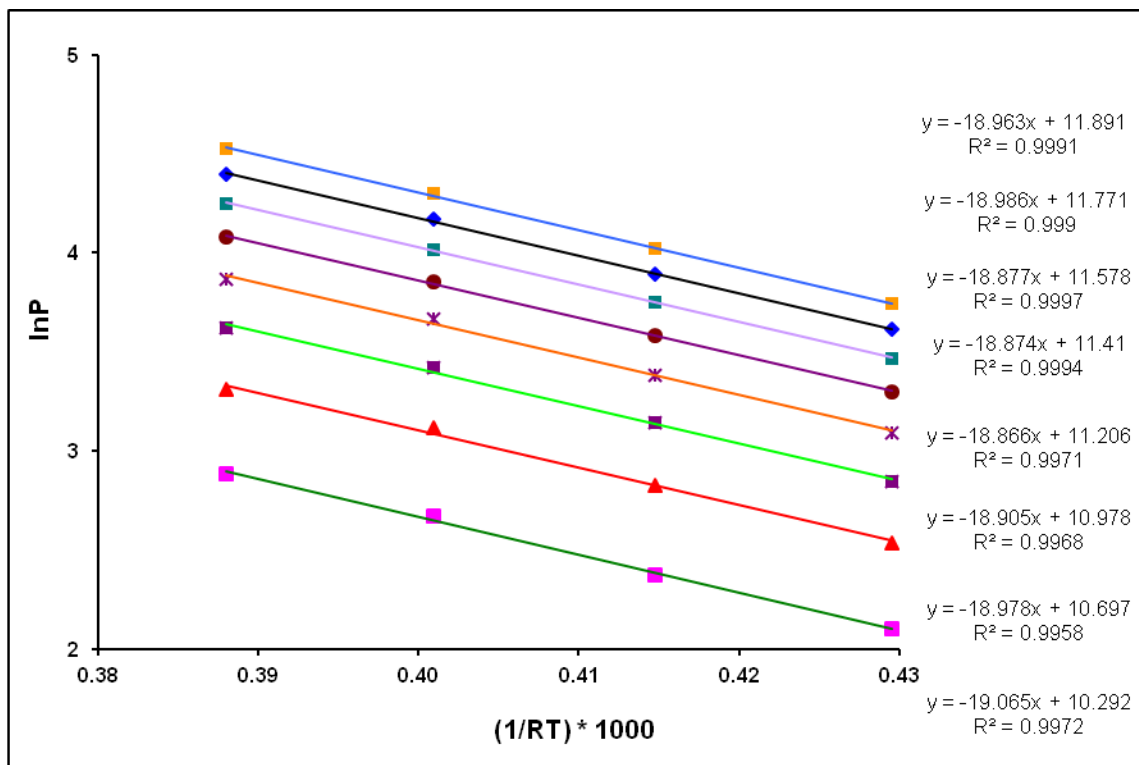


Figure S4. lnP versus 1/RT plots for different loadings for Xe adsorption in Cu^I-MFU-4l.

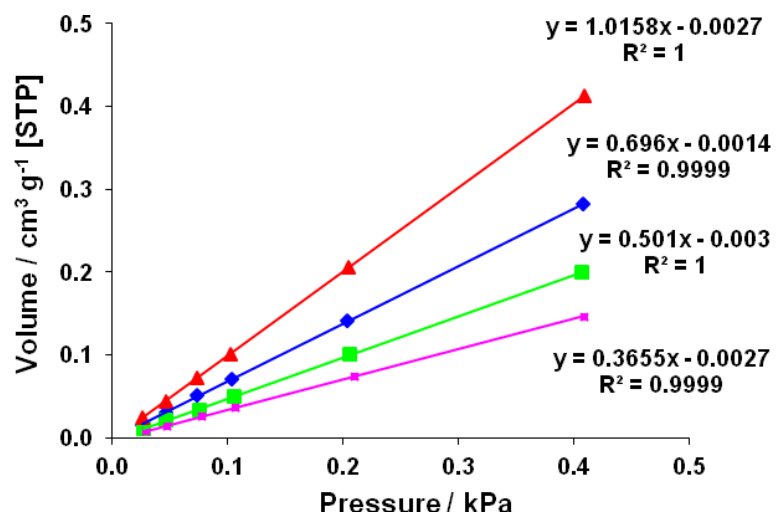


Figure S5. Determination of Henry's constants for Kr adsorption in Cu^I-MFU-4l.

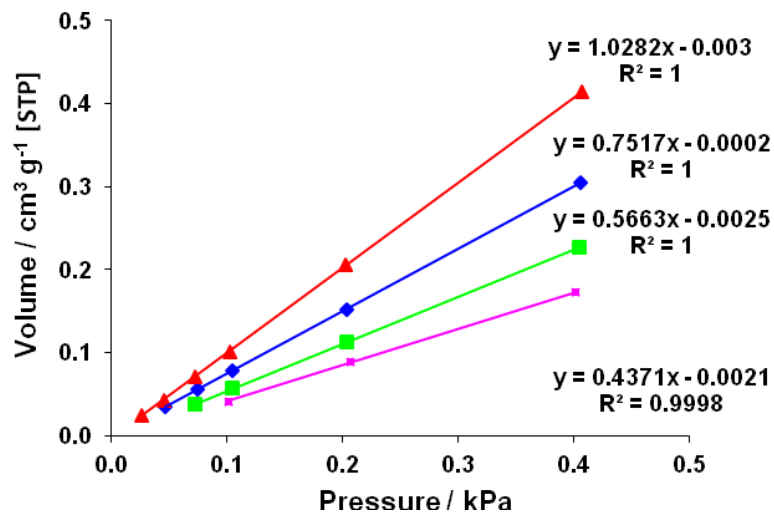


Figure S6. Determination of Henry's constants for Xe adsorption in Cu^I-MFU-4*l*.

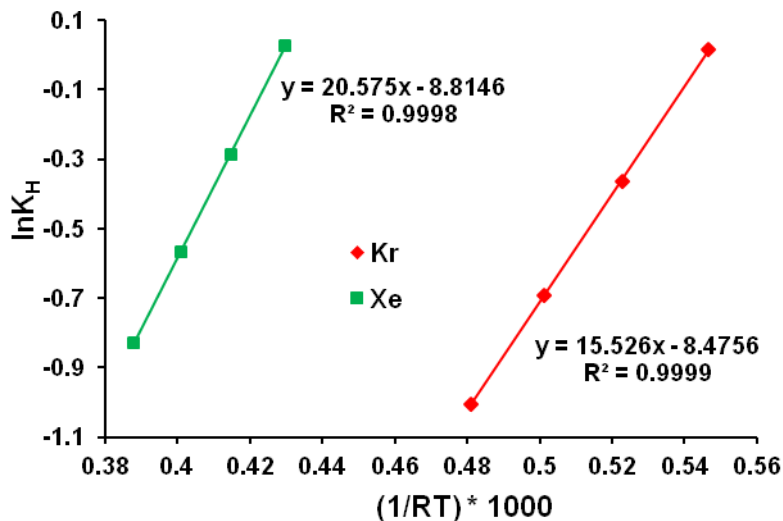


Figure S7. lnK_H versus 1/RT plots for Kr (red) and Xe (green) adsorption in Cu^I-MFU-4*l*.

The maximal selectivity of adsorption can be obtained from Henry's constants: $S_{Xe/Kr} = K_H(Xe)/K_H(Kr)$. From the linear plots, shown in Fig. S7, we can estimate $K_H(Xe)$ at 250 K ($2.9576 \text{ cm}^3 \text{ g}^{-1} \text{ kPa}^{-1}$) as well as $K_H(Kr)$ at 280 K ($0.1643 \text{ cm}^3 \text{ g}^{-1} \text{ kPa}^{-1}$). Thus, the maximal Xe/Kr selectivity will be 8.1 at 250 K and 6.3 at 280 K.

Thermal Desorption Spectroscopy of Xe and Kr in Cu^I-MFU-4l

Thermal Desorption Spectroscopy (TDS) is an analytical method to detect gas desorption from a material during heating. The in-house build TDS device with a low temperature cooling stage is described by Panella et al. and used for hydrogen desorption measurements.¹ For these investigations we operated the cooling stage with liquid nitrogen and changed the quadrupole mass spectrometer to a device allowing to detect masses up to 200amu (Microvision2, MKS Spectra Products).

Firstly, the sample (approx. 2.5mg) was activated by heating to 453K for one hour under high vacuum (10^{-6} mbar). Afterwards, the sample was exposed to a xenon (99.99%) or krypton (99.99%) atmosphere for different loading pressures at 298K for 10 minutes. Then the sample was cooled quickly down to approximately 85K under noble gas atmosphere. At this temperature the non-adsorbed gas was pumped out. Afterwards the specimen was heated with a constant heating rate of 0.1K/s under high vacuum and the desorbed gas was detected by a quadrupole mass spectrometer. Owing to the naturally occurring isotopes for krypton mass numbers 82,83,84,86 and for xenon 129,131,132,134,136 have been analyzed and the sum of the corresponding signals is given as a desorption rate.

Figure S8 shows the desorption spectra of Cu^I-MFU-4l after exposure to different pressures of xenon in the temperature range from 80K to 230K. The measurement was continued up to 300K, however no significant desorption of xenon was observed above 200K. In general for all loading pressures two distinct maxima are observed around 130K and 180K. The fluctuating signal below 115K is caused by liquid or solid xenon on the outer surface and between the powder particles during cooling to 85K.

¹ Panella, B.; Hirscher, M.; Ludescher, B.: Low-temperature thermal-desorption mass spectroscopy applied to investigate the hydrogen adsorption on porous materials. *Microporous and Mesoporous Materials* 2007, 103, 230-234.

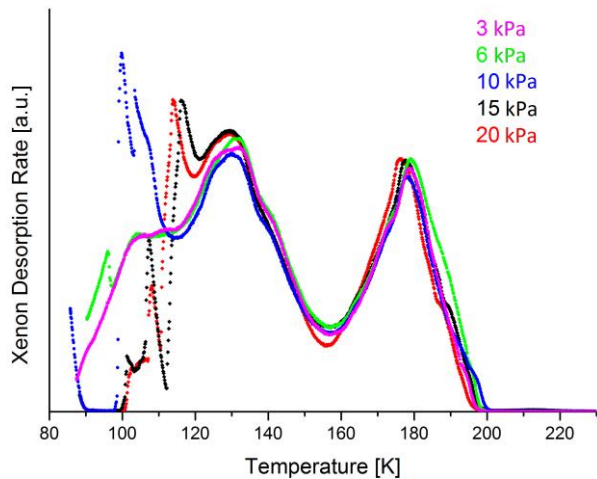


Figure S8. Xenon desorption of Cu^I-MFU-4*l* recorded with TDS for different pressures.

The desorption spectra of krypton in Cu^I-MFU-4*l* show two maxima around 95K and 120K independent of the loading pressure (Figure S9). All gas is desorbed at about 155K.

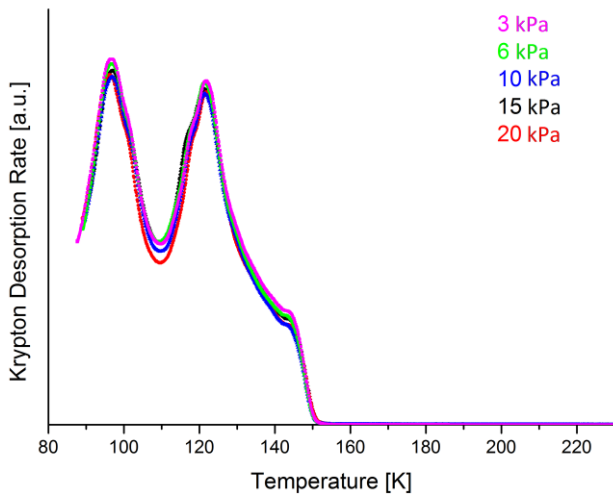


Figure S9. Krypton desorption of Cu^I-MFU-4*l* recorded with TDS for different pressures.

Both gases reveal two distinct maxima. The desorption temperature correlates with the binding strength of the noble gas atoms and therefore the maximum at lower temperature can be attributed to the second adsorbed layer or pore filling, whereas the maximum at higher temperature corresponds to the first adsorbed layer of the framework. The temperature shift of the spectra between xenon and krypton and the 50K difference in final desorption temperature are due to the different heat of adsorption. This big difference can be used for separation of xenon and krypton by a temperature-swing process.

Table S4. Lattice parameters and total amount of adsorbed atoms per unit cell for Xe adsorption in Cu^I-MFU-4I.

Temperature, K	Pressure, kPa	Lattice parameter a, Å	Total amount of Xe per UC
250	0	31.2517(3)	0
	5	31.2256(3)	2.8(2)
	10	31.2209(3)	6.0(2)
	25	31.2122(4)	16.6(7)
	50	31.2018(4)	27.9 (7)
	100	31.1813(4)	49.9(3)
170	5	31.2034(2)	64.4(3)
	10	31.1764(3)	145.2(3)
	25	31.1913(2)	261.0(3)
	50	31.1832(5)	279(1)

Table S5. Lattice parameters and total amount of adsorbed atoms per unit cell for Kr adsorption in Cu^I-MFU-4I.

Temperature, K	Pressure, kPa	Lattice parameter a, Å	Total amount of Kr per UC

250	0	31.2517(3)	0
	50	31.2443(3)	3.4(2)
	100	31.2375(3)	7.0(2)
170	5	31.2266(5)	12.0(2)
	10	31.2268(4)	18.0(2)
	25	31.2275(4)	35(1)
	50	31.2327(3)	51.9(3)
	100	31.2331(3)	84.4(3)
130	5	31.2319(5)	53.7(3)
	10	31.2219(4)	77.8(3)
	25	31.1995(4)	170.4(6)
	50	31.1979(5)	238(2)
	100	31.2090(6)	297(2)

Table S6. Atomic positions and occupancies of intercalated Xe atoms in Cu^I-MFU-4I.

T, K	p, kPa	Xe1 x,y,z,Occ	Xe2 x,y,z,Occ	Xe3 x,y,z,Occ	Xe4 x,y,z,Occ	Xe5 x,y,z,Occ	Xe6 x,y,z,Occ	Xe7 x,y,z,Occ	Xe8 x,y,z,Occ	Xe9 x,y,z,Occ	Xe10 x,y,z,Occ
Multiplicity		32	96	32	48	96	32	24	4	48	24
250	5	0.3377(9) 0.3377(9) 0.3377(9) 0.089(4)									
	10	0.3373(4) 0.3373(4) 0.3373(4) 0.188(4)									
	25	0.3370(4) 0.3370(4) 0.3370(4) 0.26(5)	0.140(4) 0.312(5) 0.140(4) 0.05(2)	0.3687(7) 0.3687(7) 0.1313(7) 0.108(3)							
	50	0.3379(4) 0.3379(4) 0.3379(4) 0.41(2)	0.127(2) 0.304(2) 0.127(2) 0.062(6)	0.3685(5) 0.3685(5) 0.1315(5) 0.190(4)	0.1808(8) 0 0.3192(8) 0.057(4)						
	100	0.3400(2) 0.3400(2) 0.3400(2) 0.682(8)	0.0996(8) 0.277(2) 0.0996(8) 0.096(4)	0.3676(5) 0.3676(5) 0.1324(5) 0.258(5)	0.171(1) 0 0.329(1) 0.089(5)	0.087(2) 0 0 0.066(4)					
170	5	0.3377(1) 0.3377(1) 0.3377(1) 0.900(8)	0.0952(8) 0.269(1) 0.0952(8) 0.091(5)	0.3653(3) 0.3653(3) 0.1347(3) 0.439(7)	0.1723(8) 0 0.3277(8) 0.134(5)	0.083(1) 0 0 0.067(3)					
	10	0.3383(2) 0.3383(2) 0.3383(2) 0.922(9)	0.0873(3) 0.2711(3) 0.0873(3) 0.408(6)	0.3662(4) 0.3662(4) 0.1338(4) 0.463(7)	0.1688(3) 0 0.3312(3) 0.480(7)	0.0928(4) 0 0 0.282(4)	0.0664(4) -0.0664(4) 0.5664(4) 0.274(5)	0 0 0.327(2) 0.119(6)			
	25	0.3362(2) 0.3362(2) 0.3362(2) 0.85(1)	0.0896(2) 0.2569(3) 0.0896(2) 0.652(6)	0.3645(5) 0.3645(5) 0.1355(5) 0.473(9)	0.1682(2) 0 0.3318(5) 0.880(7)	0.0768(4) -0.0804(3) 0.5804(3) 0.594(9)	0.0804(3) -0.0804(3) 0.3457(5) 0.73(1)	0 0 0.5 0.80(2)	-0.1255(2) 0 0.8746(2) 0.700(9)	-0.093(1) 0 0 0.297(7)	
	50	0.3391(4) 0.3391(4) 0.3391(4) 0.89(2)	0.0894(3) 0.2547(5) 0.0894(3) 0.66(2)	0.3722(9) 0.3722(9) 0.1278(9) 0.477(2)	0.1665(3) 0 0.3335(3) 0.98(1)	0.0721(8) -0.0823(4) 0.5823(4) 0.34(2)	0.0823(4) -0.0823(4) 0.335(1) 0.73(2)	0 0 0.5 0.83(3)	-0.1219(3) 0 0.8782(3) 0.77(2)	-0.074(2) 0 0 0.35(1)	

Table S7. Atomic positions and occupancies of intercalated Kr atoms in Cu^I-MFU-4I.

T, K	p, kPa	Kr1 x,y,z,Occ	Kr2 x,y,z,Occ	Kr3 x,y,z,Occ	Kr4 x,y,z,Occ	Kr5 x,y,z,Occ	Kr6 x,y,z,Occ	Kr7 x,y,z,Occ	Kr8 x,y,z,Occ
Multiplicity	32	96	32	48	96	32	24	4	
250	50	0.3365 (8) 0.3365 (8) 0.3365 (8) 0.105 (4)							
	100	0.3367 (4) 0.3367 (4) 0.3367 (4) 0.220 (5)							
170	5	0.3339 (3) 0.3339 (3) 0.3339 (3) 0.375 (6)							
	10	0.3342 (2) 0.3342 (2) 0.3342 (2) 0.563 (6)							
	25	0.3335 (3) 0.3335 (3) 0.3335 (3) 0.54 (3)	0.1362 (2) 0.2989 (2) 0.1362 (2) 0.094 (9)	0.369 (1) 0.369 (1) 0.131 (1) 0.117 (5)	0.201 (1) 0.5 0.299 (1) 0.108 (5)				
	50	0.3352 (2) 0.3352 (2) 0.3352 (2) 0.859 (8)	0.095 (8) 0.267 (1) 0.095 (8) 0.120 (4)	0.3685 (7) 0.3685 (7) 0.1315 (7) 0.180 (6)	0.1866 (8) 0 0.3134 (8) 0.149 (5)				
	100	0.3355 (2) 0.3355 (2) 0.3355 (2) 0.918 (9)	0.0965 (5) 0.2693 (6) 0.0965 (5) 0.226 (5)	0.3692 (5) 0.3692 (5) 0.1308 (5) 0.272 (6)	0.1738 (5) 0 0.3262 (5) 0.254 (6)	0.0943 (8) 0.1942 (9) 0 0.129 (4)			
130	5	0.3335 (2) 0.3335 (2) 0.3335 (2) 0.990 (8)	0.094 (1) 0.263 (2) 0.094 (1) 0.096 (5)	0.3686 (6) 0.3686 (6) 0.1314 (6) 0.219 (6)	0.190 (1) 0 0.310 (1) 0.121 (6)				
	10	0.3342 (2) 0.3342 (2) 0.3342 (2) 0.99 (1)	0.0999 (6) 0.2663 (8) 0.0999 (6) 0.194 (5)	0.3676 (6) 0.3676 (6) 0.1324 (6) 0.290 (7)	0.1757 (7) 0 0.3243 (7) 0.211 (6)	0.088 (2) 0.198 (2) 0 0.084 (4)			
	25	0.3365 (2) 0.3365 (2) 0.3365 (2) 1.00 (2)	0.1000 (3) 0.2653 (3) 0.1000 (3) 0.596 (8)	0.3696 (4) 0.3696 (4) 0.1304 (4) 0.53 (1)	0.1708 (4) 0 0.3292 (4) 0.625 (9)	0.1027 (5) 0.1724 (6) 0 0.356 (5)			
	50	0.3382 (4) 0.3382 (4) 0.3382 (4) 1.00 (5)	0.0999 (4) 0.2688 (7) 0.0999 (4) 0.68 (2)	0.3719 (8) 0.3719 (8) 0.1281 (8) 0.47 (2)	0.1618 (5) 0 0.3382 (5) 0.69 (3)	0.1012 (6) 0.1947 (5) 0 0.66 (2)	0.0831 (6) -0.0831 (6) 0.5831 (6) 0.59 (2)	0 0 0.347 (2) 0.44 (2)	
	100	0.3349 (6) 0.3349 (6) 0.3349 (6) 0.98 (3)	0.1004 (3) 0.2683 (5) 0.1004 (3) 0.83 (2)	0.3711 (8) 0.3711 (8) 0.1289 (8) 0.48 (2)	0.1636 (5) 0 0.3364 (5) 0.98 (3)	0.0924 (5) 0.1826 (6) 0 0.87 (2)	0.0903 (8) -0.0903 (8) 0.5903 (8) 0.65 (3)	0 0 0.369 (2) 0.76 (3)	0 0 0.5 0.19 (8)

Rietveld plots of Cu^I-MFU-4l with different amount of adsorbed Xe and Kr

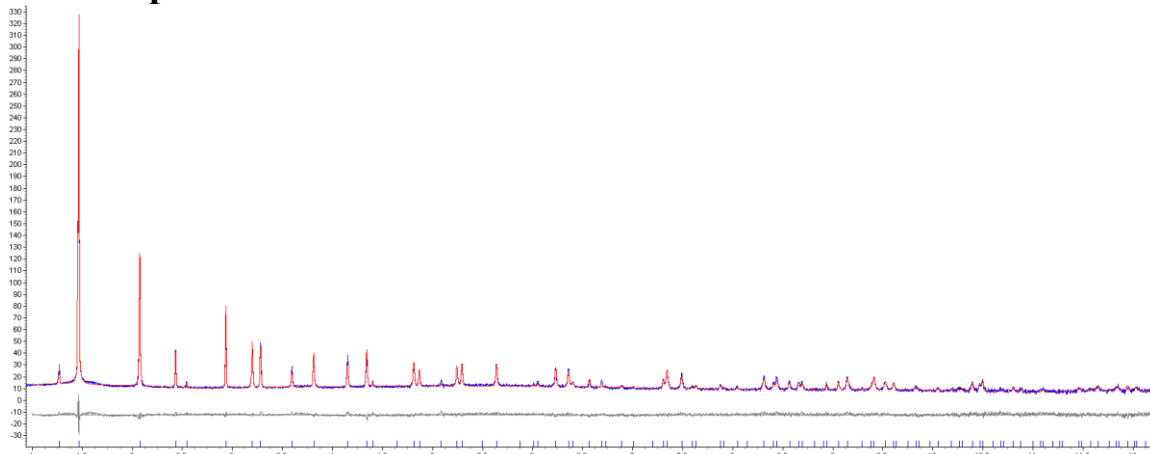


Figure S10. Rietveld plot of Cu^I-MFU-4l with 5 kPa of Xe, 250K. Y-axis scale – square root of X-ray counts for better visibility of low-intensity reflections.

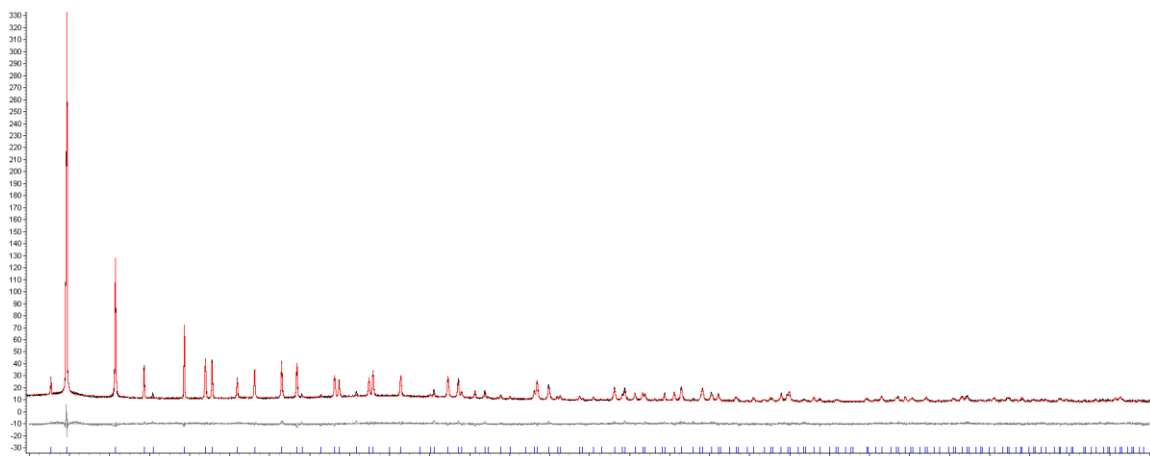


Figure S11. Rietveld plot of Cu^I-MFU-4l with 10 kPa of Xe, 250K. Y-axis scale – square root of X-ray counts for better visibility of low-intensity reflections.

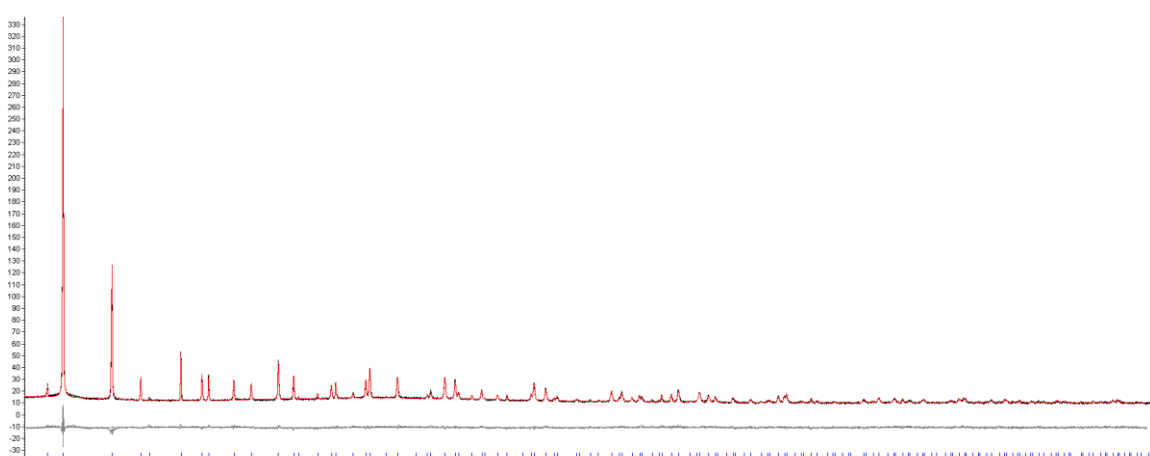


Figure S12. Rietveld plot of Cu^I-MFU-4l with 25 kPa of Xe, 250K. Y-axis scale – square root of X-ray counts for better visibility of low-intensity reflections.

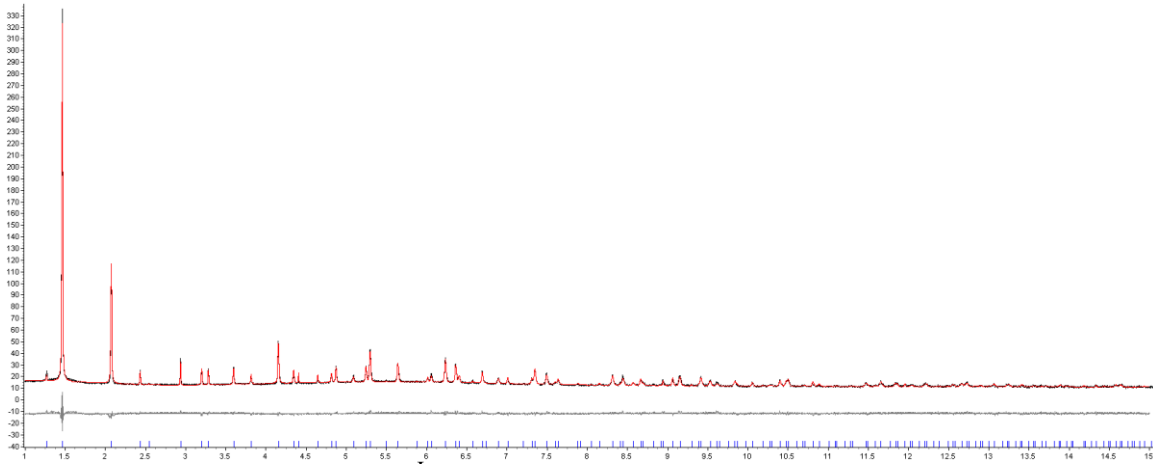


Figure S13. Rietveld plot of Cu^I-MFU-4l with 50 kPa of Xe, 250K. Y-axis scale – square root of X-ray counts for better visibility of low-intensity reflections.

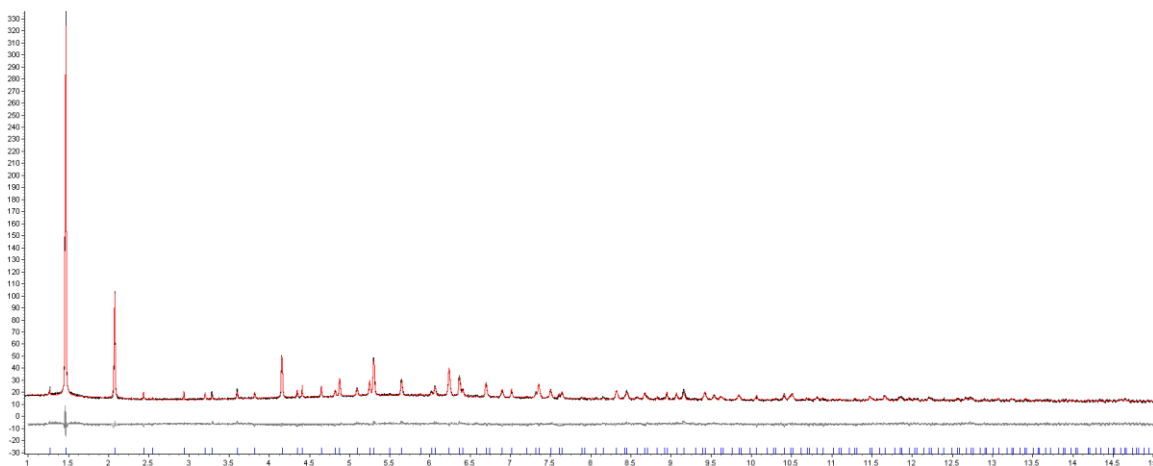


Figure S14. Rietveld plot of Cu^I-MFU-4l with 100 kPa of Xe, 250K. Y-axis scale – square root of X-ray counts for better visibility of low-intensity reflections.

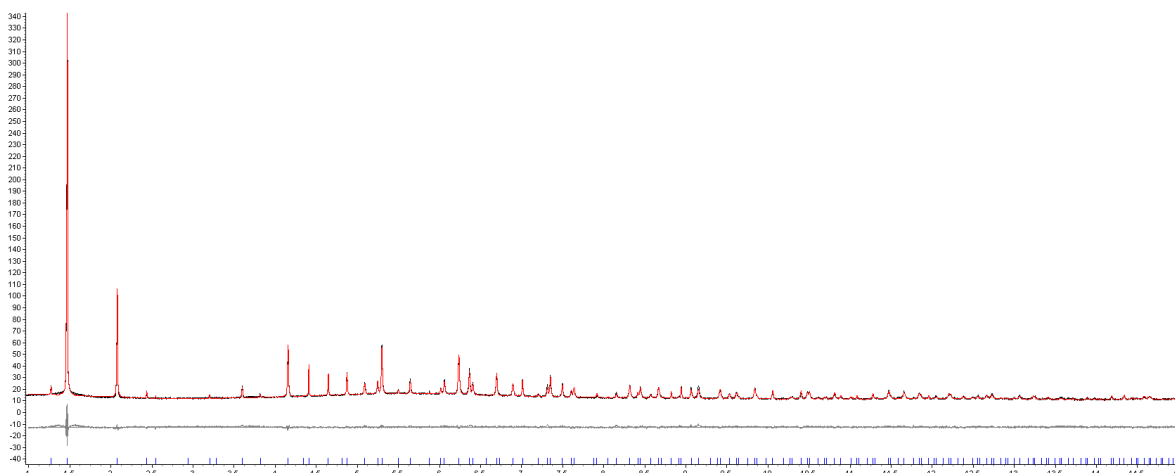


Figure S15. Rietveld plot of Cu^I-MFU-4l with 5 kPa of Xe, 170K. Y-axis scale – square root of X-ray counts for better visibility of low-intensity reflections.

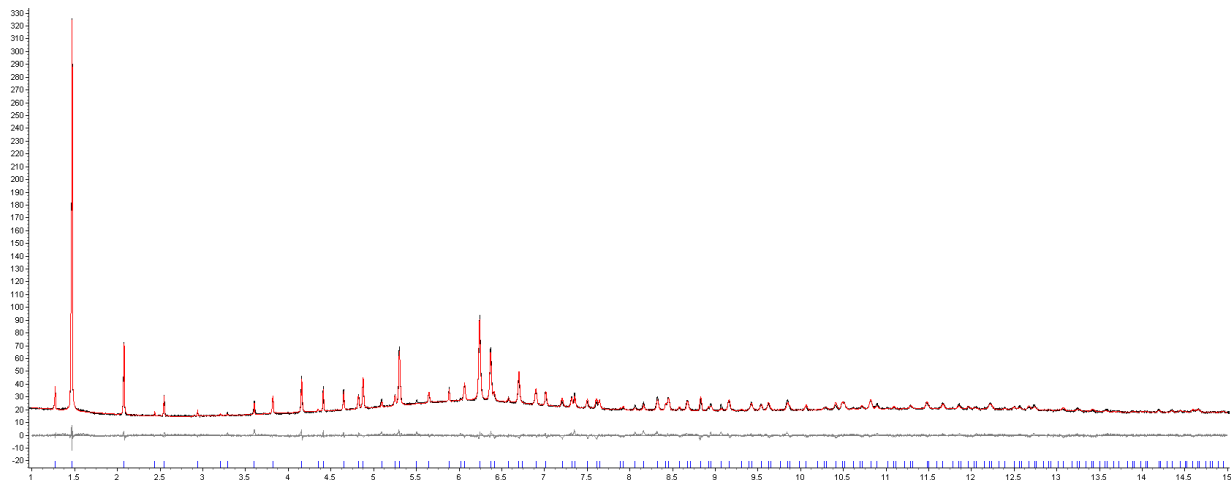


Figure S16. Rietveld plot of Cu^I-MFU-4l with 10 kPa of Xe, 170K. Y-axis scale – square root of X-ray counts for better visibility of low-intensity reflections.

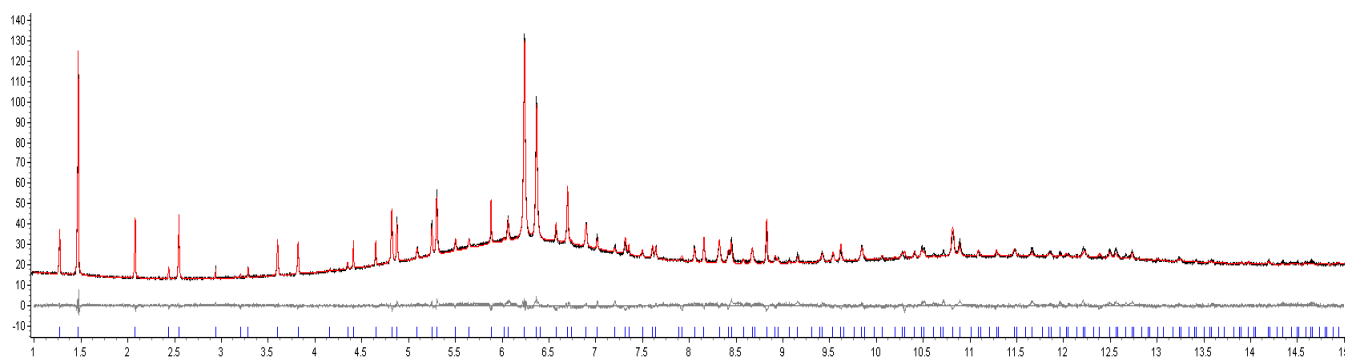


Figure S17. Rietveld plot of Cu^I-MFU-4l with 25 kPa of Xe, 170K. Y-axis scale – square root of X-ray counts for better visibility of low-intensity reflections.

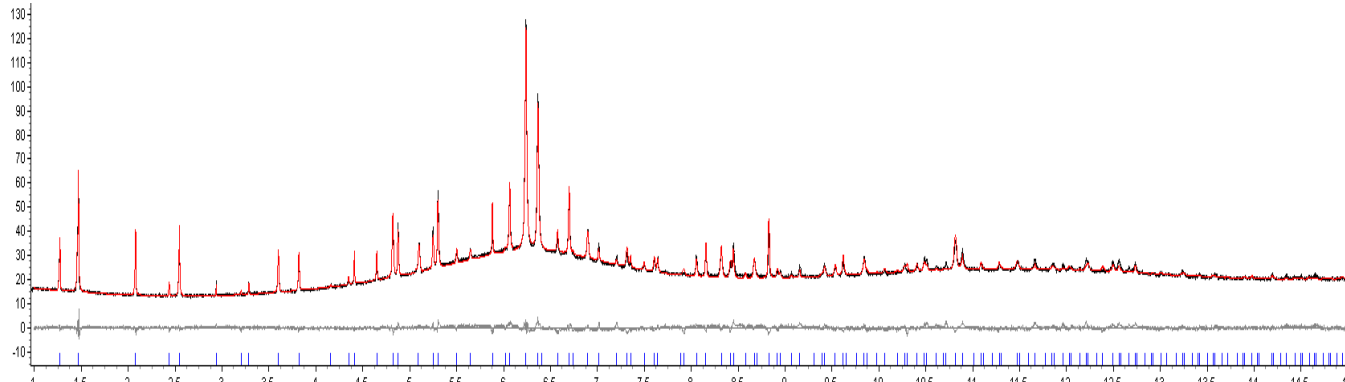


Figure S18. Rietveld plot of Cu^I-MFU-4l with 50 kPa of Xe, 170K. Y-axis scale – square root of X-ray counts for better visibility of low-intensity reflections.

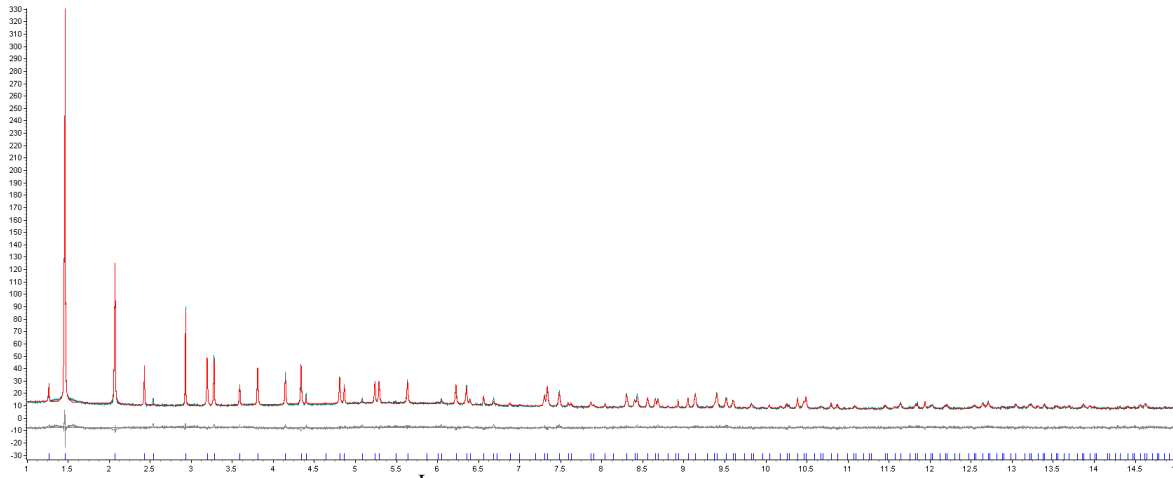


Figure S19. Rietveld plot of Cu^I-MFU-4l with 50 kPa of Kr, 250K. Y-axis scale – square root of X-ray counts for better visibility of low-intensity reflections.

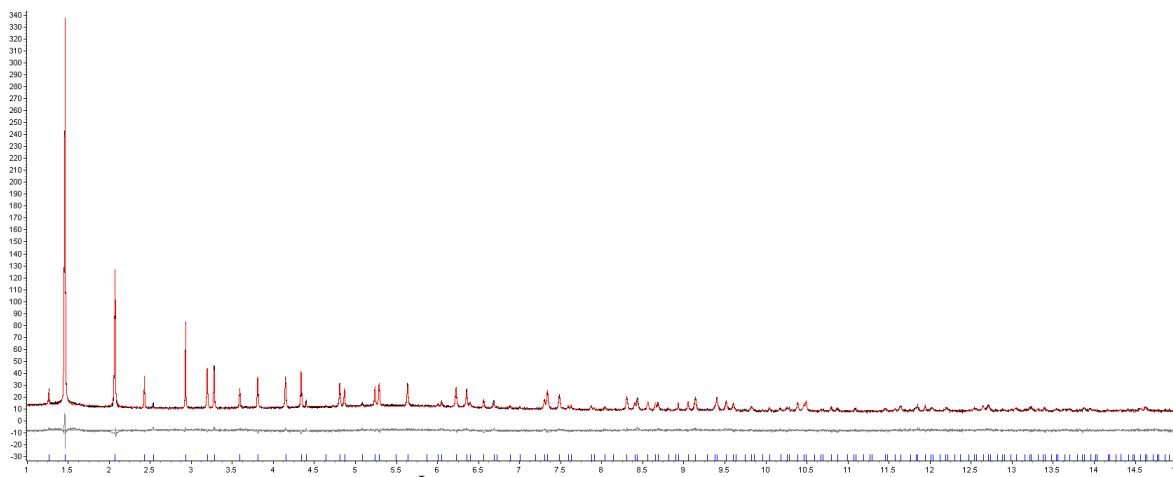


Figure S20. Rietveld plot of Cu^I-MFU-4l with 100 kPa of Kr, 250K. Y-axis scale – square root of X-ray counts for better visibility of low-intensity reflections.

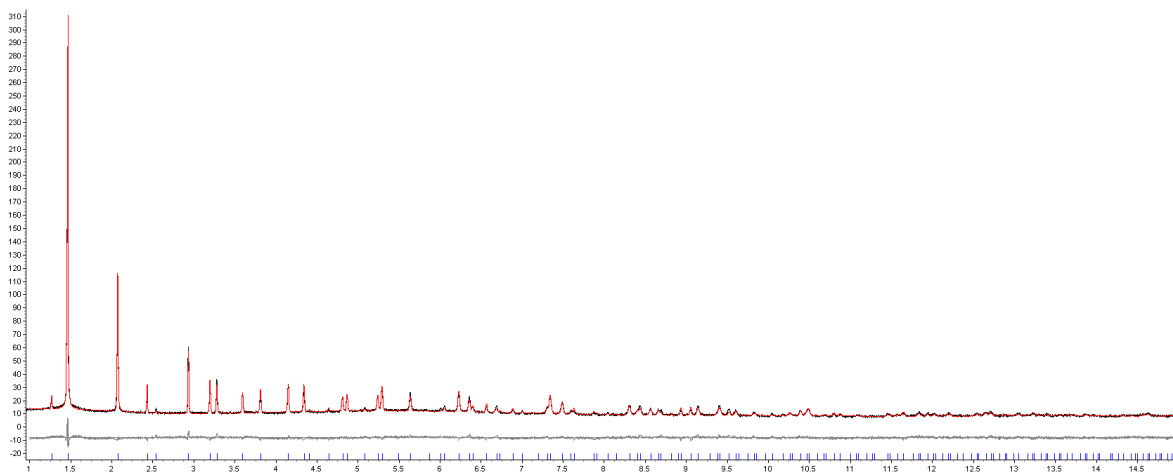


Figure S21. Rietveld plot of Cu^I-MFU-4l with 5 kPa of Kr, 170K. Y-axis scale – square root of X-ray counts for better visibility of low-intensity reflections.

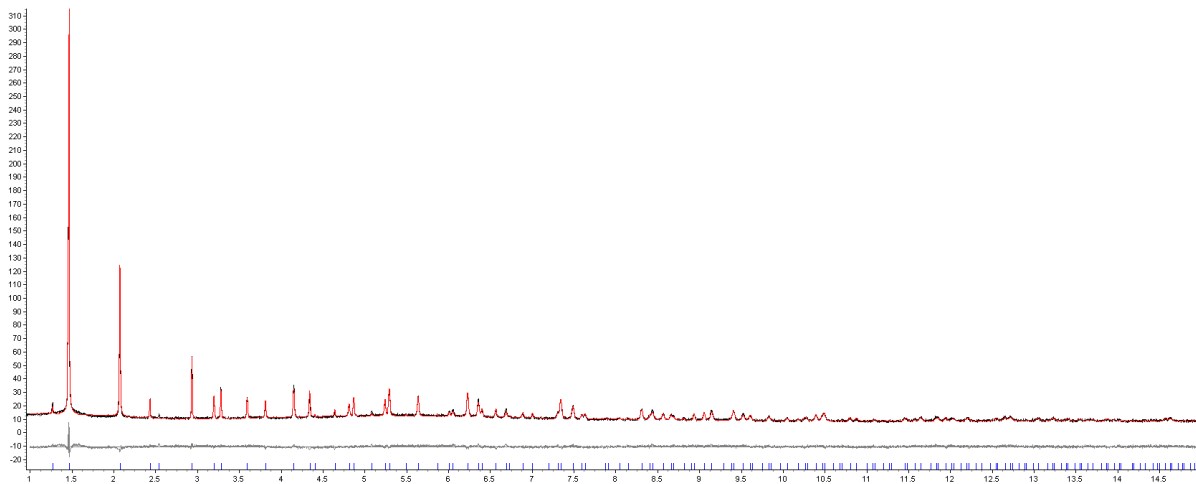


Figure S22. Rietveld plot of Cu^I-MFU-4l with 10 kPa of Kr, 170K. Y-axis scale – square root of X-ray counts for better visibility of low-intensity reflections.

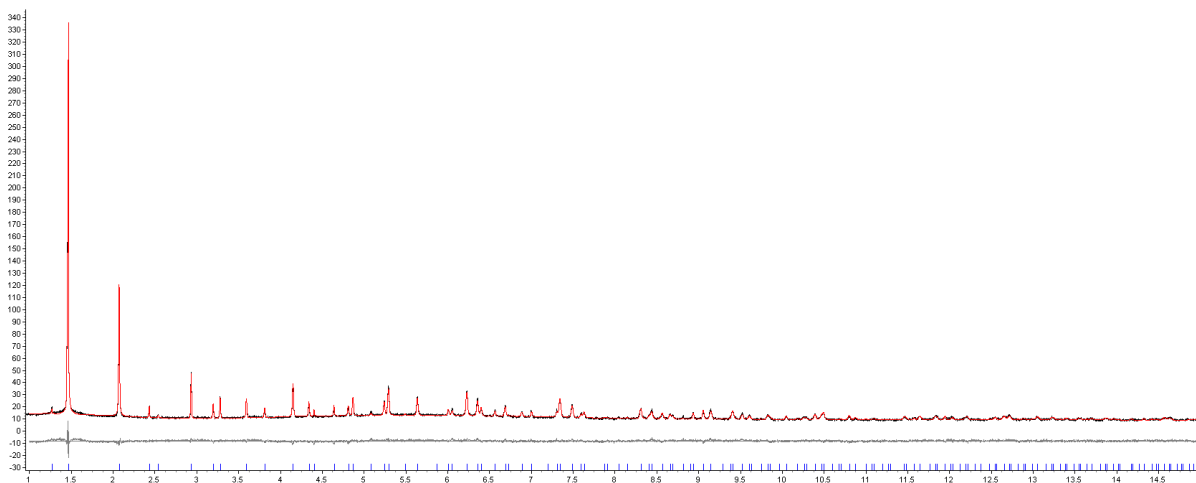


Figure S23. Rietveld plot of Cu^I-MFU-4l with 25 kPa of Kr, 170K. Y-axis scale – square root of X-ray counts for better visibility of low-intensity reflections.

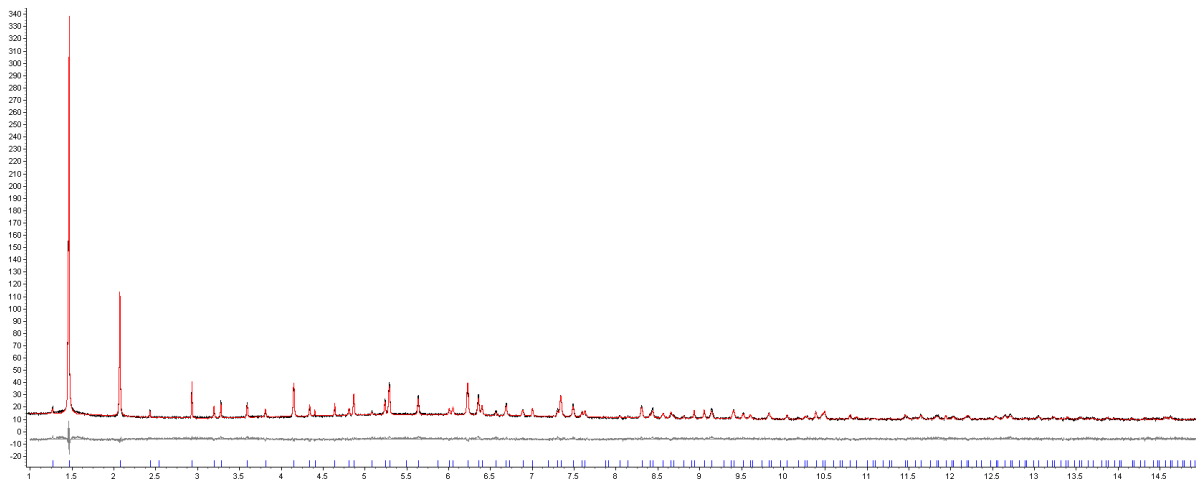


Figure S24. Rietveld plot of Cu^I-MFU-4l with 50 kPa of Kr, 170K. Y-axis scale – square root of X-ray counts for better visibility of low-intensity reflections.

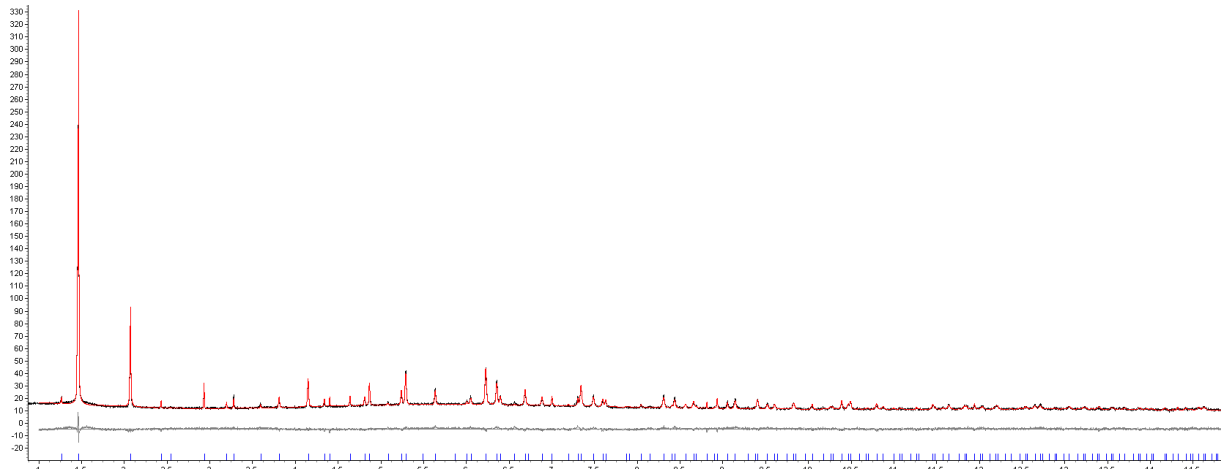


Figure S25. Rietveld plot of Cu^I-MFU-4l with 100 kPa of Kr, 170K. Y-axis scale – square root of X-ray counts for better visibility of low-intensity reflections.

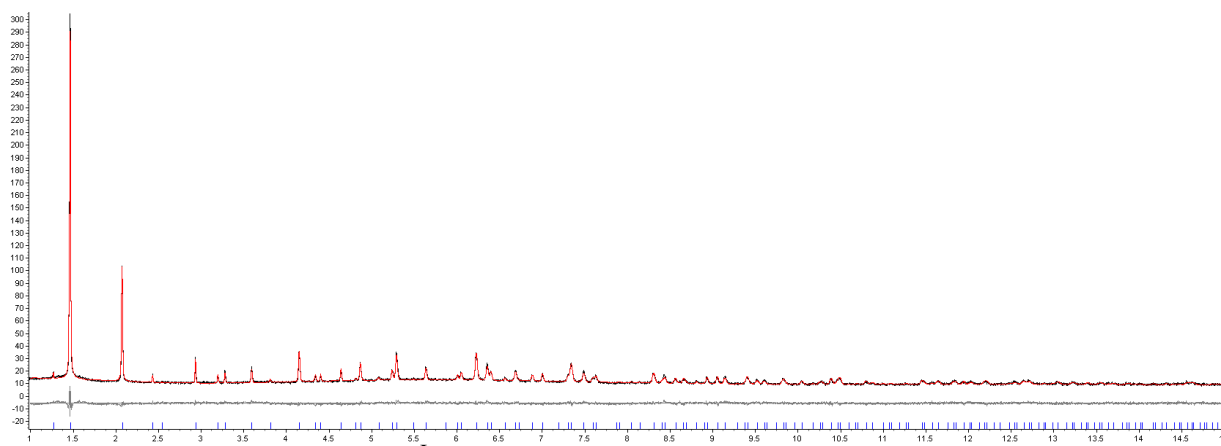


Figure S26. Rietveld plot of Cu^I-MFU-4l with 5 kPa of Kr, 130K. Y-axis scale – square root of X-ray counts for better visibility of low-intensity reflections.

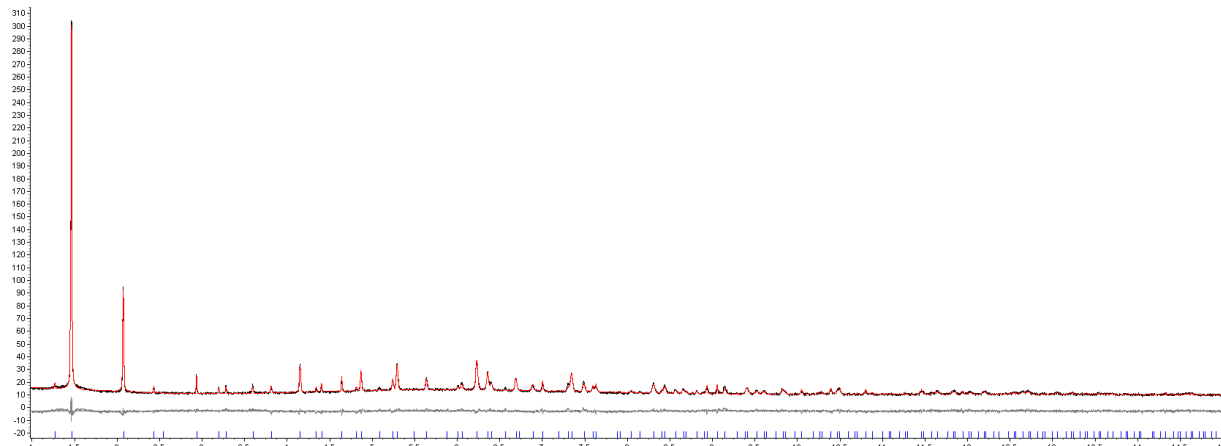


Figure S27. Rietveld plot of Cu^I-MFU-4l with 10 kPa of Kr, 130K. Y-axis scale – square root of X-ray counts for better visibility of low-intensity reflections.

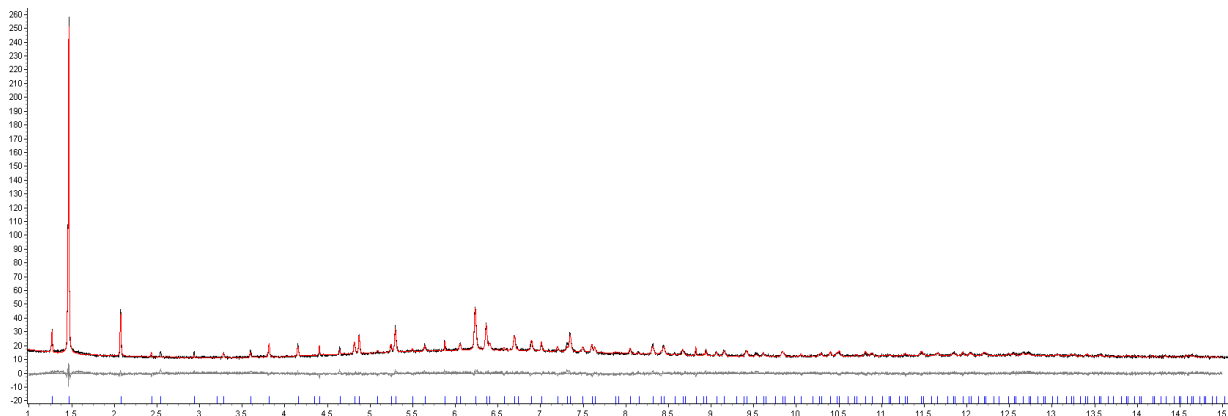


Figure S28. Rietveld plot of $\text{Cu}^{\text{I}}\text{-MFU-4l}$ with 25 kPa of Kr, 130K. Y-axis scale – square root of X-ray counts for better visibility of low-intensity reflections.

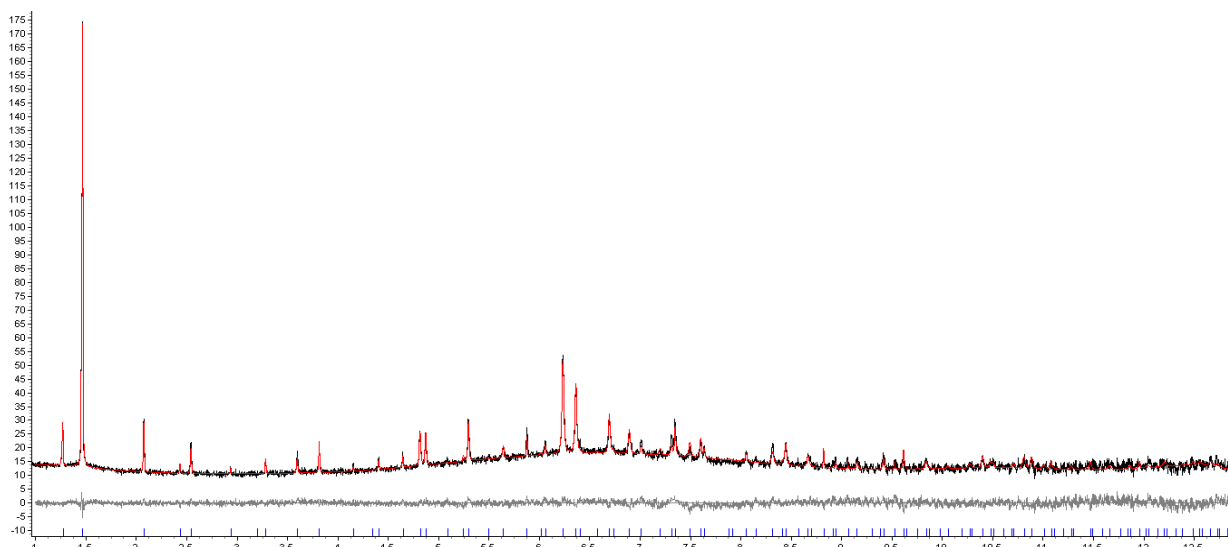


Figure S29. Rietveld plot of $\text{Cu}^{\text{I}}\text{-MFU-4l}$ with 50 kPa of Kr, 130K. Y-axis scale – square root of X-ray counts for better visibility of low-intensity reflections.

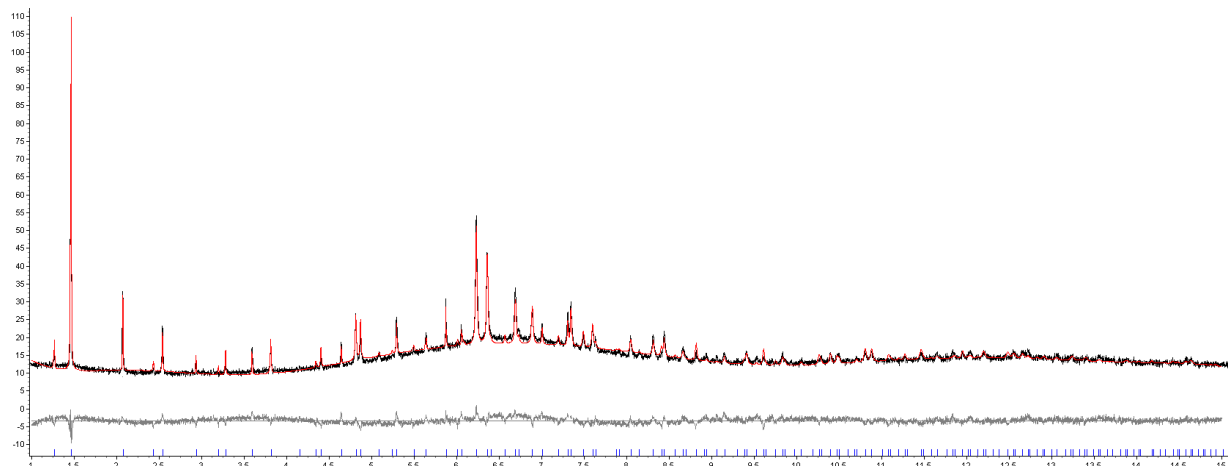


Figure S30. Rietveld plot of $\text{Cu}^{\text{I}}\text{-MFU-4l}$ with 100 kPa of Kr, 130K. Y-axis scale – square root of X-ray counts for better visibility of low-intensity reflections.